Reversible Ferromagnetic Phase Transition in Electrode-Gated Manganites

Bin Cui, Cheng Song, Guangyue Wang, Yinuo Yan, Jingjing Peng, Jinghui Miao, Haijun Mao, Fan Li, Chao Chen, Fei Zeng, and Feng Pan**

The electronic phase transition has been considered as a dominant factor in the phenomena of colossal magnetoresistance, metal-insulator transition, and exchange bias in correlated electron systems. However, the effective manipulation of the electronic phase transition has remained a challenging issue. Here, the reversible control of ferromagnetic phase transition in manganite films through ionic liquid gating is reported. Under different gate voltages, the formation and annihilation of an insulating and magnetically hard phase in the magnetically soft matrix, which randomly nucleates and grows across the film instead of initiating at the surface and spreading to the bottom, is directly observed. This discovery provides a conceptually novel vision for the electric-field tuning of phase transition in correlated oxides. In addition to its fundamental significance, the realization of a reversible metal-insulator transition in colossal magnetoresistance materials will also further the development of four-state memories, which can be manipulated by a combination of electrode gating and the application of a magnetic field.

1. Introduction

The modification of electronic phases in correlated oxides is one of the core issues of condensed matter.[1,2] Electronic phase separation introduces phases with different electron densities and leads to numerous fascinating phenomena.[3–5] In mixed-valence manganites, the lateral electronic phase separation is sensitive to the hole doping concentration, the temperature, and even some unintentional factors, making the nano-scale characterization and quantitative control of lateral electronic phase separation quite a challenging task.[3,6] The vertical phase separation is expected to be more feasible for electronic structure modification by strain engineering.[5,7] However, chemical doping and lattice distortion inevitably introduce impurities and extra scattering centers to the system, which worsen the performances of the manganites. Moreover, these processes are irreversible and hardly controllable, thus limiting their practical applications in information storage.

Electric-field gating offers an effective route to confine electrons in nanoscale regions.[2,8] Compared with the conventional electric current control of magnetism, such as spin transfer torque, which needs a current density of 10^6 A/cm^2, electric-field-induced magnetization is expected to dramatically reduce the power consumption in data storage devices.[2,9] The application of voltages via a gate electrode has been reported to successfully control the coercivity, saturation magnetization, and Curie temperature (T_C) of magnetic materials by electron density variation or even by electronic phase transition (PT).[10–12] The origin of such a transition has been vigorously pursued, with several mechanisms proposed to date: surface carrier density modulation, oxygen vacancies formation, and internal carrier localization.[13–15] Among these mechanisms, the field-effect-induced oxygen vacancies, unlike mechanisms that are electrostatic in origin, is a unique approach to realizing the stable carrier density modulation even when the gate voltage is removed.[14] However, a conclusive mechanism for this phase transition remains under debate and long-term challenges for this rather contradictory situation are that the electronic PT is difficult to be directly observed and the entanglement between electric field penetration and PT is complicated.[16,17] More problematic, such a standstill in mechanism not only covers the rich spectrum of PT during extreme metal-insulator transition but also hampers the achievement of reversible PT with robust phases, which is vital to the electrical cycle characteristics of a field-effect device. In this work, we succeed in directly observing the formation and annihilation of an insulating and magnetically hard phase in the soft magnetic matrix in electrode-gated manganites, where a combination of electric and magnetic fields realizes a four-state memory system.

2. Results and Discussion

We investigated the dependence of T_C and magnetoresistance (MR) on gate voltages (V_G) in the 20-nm-thick high-quality $La_{0.6}Sr_{0.4}MnO_3$ (LSMO) Hall bar gated by ionic liquid (more

B. Cui, Dr. C. Song, G. Y. Wang, Y. N. Yan, J. J. Peng, J. H. Miao, H. J. Mao, F. Li, Dr. C. Chen, Dr. F. Zeng, Prof. F. Pan
Key Laboratory of Advanced Materials (MOE)
School of Materials Science and Engineering
Tsinghua University
Beijing, 100084, China
E-mail: songcheng@mail.tsinghua.edu.cn; panf@mail.tsinghua.edu.cn

DOI: 10.1002/adfm.201402007

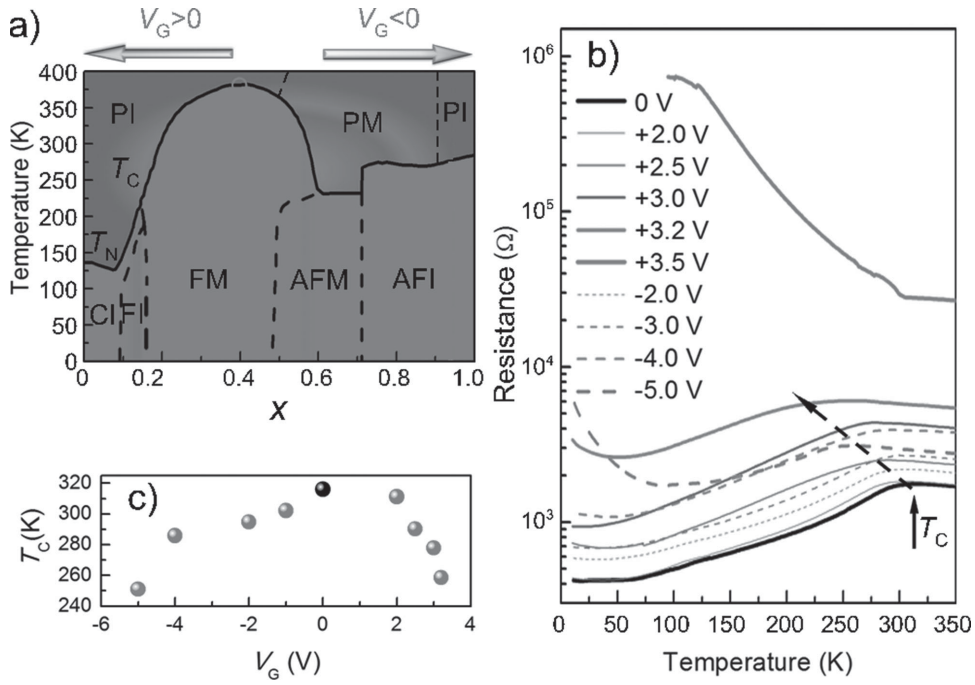

Figure 1. a) Electronic phase diagram of $La_{1-x}Sr_xMnO_3$ with varying doping level *x*. The abbreviations denote spin-canted insulating (CI), ferromagnetic insulating (FI), ferromagnetic metal (FM), antiferromagnetic metal (AFM), antiferromagnetic insulating (AFI), paramagnetic insulating (PI), and paramagnetic metal (PM) phase. b) Temperature dependence of the resistance for a channel with various gate voltages. The solid and dashed arrows indicate the T_C and its tendency with V_G, respectively. c) V_G dependence of T_C.

details are provided in the Experimental Section, Figure S1,S2 in the Supporting Information). $La_{0.6}Sr_{0.4}MnO_3$ is selected due to its high T_C and extreme sensitivity to external stimuli,[18] with the possibility of irreversible reaction with ionic liquid having been carefully excluded in previous work.[15] The electronic phase diagram of $La_{1-x}Sr_xMnO_3$ is shown in **Figure 1**a, where *x* is the doping level. The channel resistance versus temperature (*R*-*T*) curves are depicted in Figure 1b, where T_C is obtained from the metal-insulator transition temperatures ($dR/dT = 0$) marked by the solid arrow. The change in T_C following V_G is denoted by the dashed arrow. The T_C values as a function of V_G are summarized in Figure 1c. The pristine LSMO (V_G = 0 V) is a ferromagnetic metal (FM) with T_C of 316 K, which somehow is lower than the ideal value for the given composition (circle in Figure 1a) but is normal for a thin manganite film.[3] In contrast to the case of V_G = +2.0 V, where the electric field effect is limited on the film surface and the FM phase dominates the channel, LSMO under a positive V_G of 3.2 V exhibits ten times the resistance enhancement accompanied by a reduced T_C of 260 K, fitting well with the tendency in the above phase diagram. With a further increase in V_G (+3.5 V), the sample sharply changes to an insulating phase irreversibly, where the electric field effect is dramatically enhanced in the completely insulating channel with a much larger screening length.[15] Note that once a positive V_G of +3.0 V is applied, the transition could only be reversed by a sizable negative voltage (Figure S3 in the Supporting Information), suggesting that the gating effect is not electrostatic in origin.[14]

On the contrary, when a negative voltage is applied, the LSMO enters into the adjacent antiferromagnetic metal (AFM) phase in the diagram, which forbids the permeation of electric field into the sample. Hence, the channel maintains metallic conductivity until a V_G as large as –5.0 V is applied. Note that there are some quantitative differences between the Sr doping and the V_G controlled phase diagram. The differences could be explained by two possible reasons: i) the phase diagram of bulk materials is somewhat different from that of thin films in our case and ii) the electronic phase transition induced by the electric field effect might not be as uniform as the scenario in which Sr doping takes the screening effect into account. Nevertheless, the tendency of the phase transition that is reflected by the variation in channel resistance and Curie temperature fits the phase diagram well. Aside from the transportation measurements of the Hall bar configuration, a 2.5 mm × 2.5 mm film sample gated by ionic liquid was used for magnetization experiments. The dependence of T_C on V_G derived from the magnetization experiments on the film sample, as presented in Figure S4 in the Supporting Information, strongly supports the result obtained from the small Hall bar. In addition, a similar electrical manipulation in $La_{0.8}Sr_{0.2}MnO_3$ indicates that the application of a negative gate voltage increases the T_C and the conductivity, while the application of a positive one reduces them (Figure S5 in the Supporting Information), reaffirming the effect of V_G on the phase transition tendency in $La_{1-x}Sr_xMnO_3$, as shown in Figure 1a.

We now turn to investigate the origin of the electronic PT. X-ray photoelectron spectroscopy (XPS) was used to analyze the film samples under different voltages, which were prepared in the same way as in magnetization measurements (Figure S6 in Supporting Information). **Figure 2** depicts the Mn 2*p* core-level spectra of the samples under varied gate voltages. The positions of the Mn $2p_{3/2}$ core-level peaks are summarized in

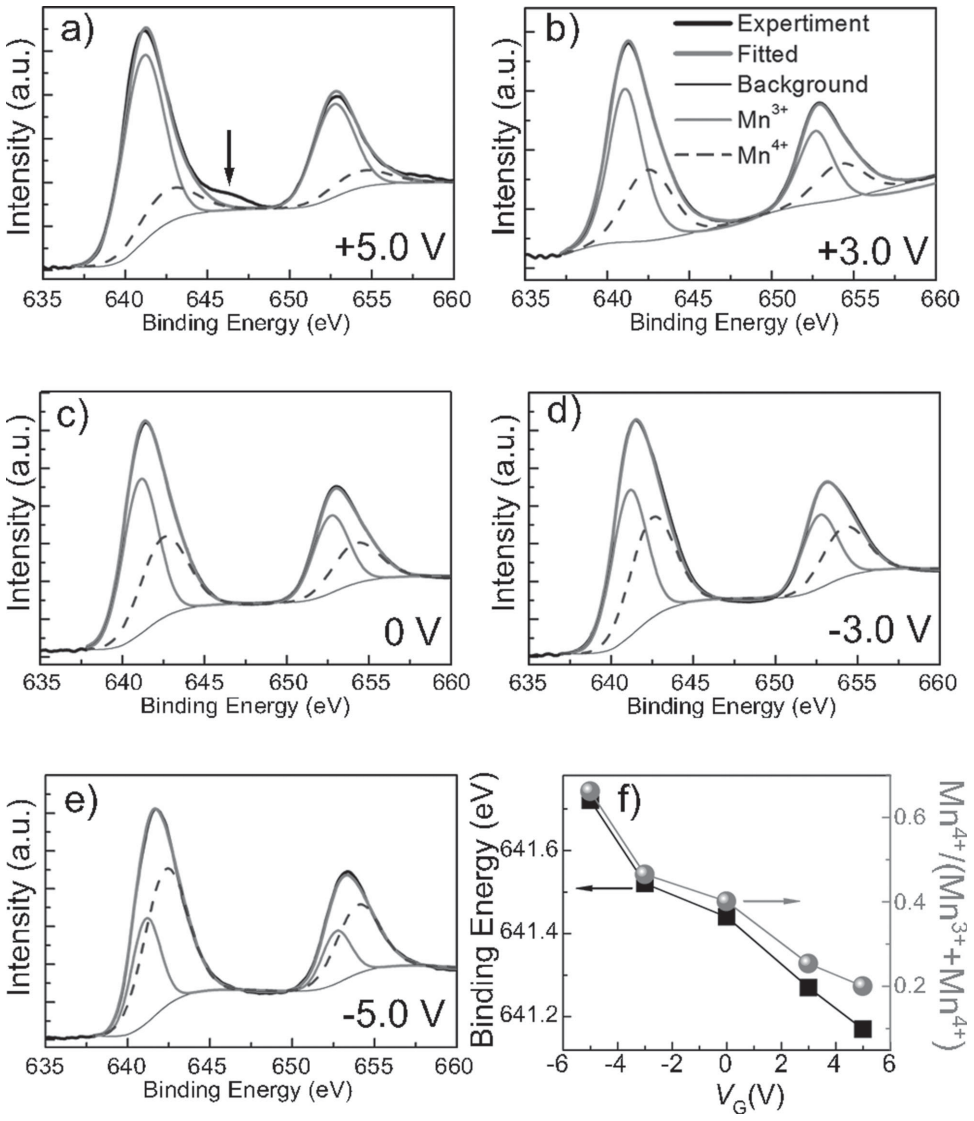

Figure 2. a–e) Mn 2*p* XPS spectra of samples with different gate voltages. f) V_G dependence of Mn $2p_{3/2}$ peak position (left axis) and $Mn^{4+}/(Mn^{3+}+Mn^{4+})$ ratio (right axis).

Figure 2f, which shift from 641.17 eV to 641.72 eV as gate voltages change from +5.0 V to –5.0 V, suggesting that the positive gating voltages decrease the $Mn^{4+}/(Mn^{3+}+Mn^{4+})$ ratio, while the negative ones do the opposite. To extract more information from the Mn valence evolution, multiple-peak fittings for the Mn 2*p* core-level spectra are performed. $LaMnO_3$ and MnO_2 spectra are used as references of the main peaks of the Mn^{3+} and Mn^{4+} states, respectively.[19,20] The proportion of the $Mn^{4+}/(Mn^{3+}+Mn^{4+})$ in the samples could then be estimated by the areas of the Mn^{3+} and Mn^{4+} peaks. The $Mn^{4+}/(Mn^{3+}+Mn^{4+})$ ratio in the pristine sample (V_G = 0 V) is approximately 0.40, which is in good agreement with the stoichiometric ratio in $La_{0.6}Sr_{0.4}MnO_3$ films. Remarkably, at V_G = +3.0 V, the $Mn^{4+}/(Mn^{3+}+Mn^{4+})$ ratio is 0.25, which is a value that is extremely close to the FM-FI phase boundary. For the extreme case of V_G = +5.0 V with the $Mn^{4+}/(Mn^{3+}+Mn^{4+})$ ratio of 0.20, a tail peak at higher binding energy due to the introduction of Mn^{2+} ions is marked by the arrow.[21] With a negative bias of –3.0 V, the $Mn^{4+}/(Mn^{3+}+Mn^{4+})$ ratio is approximately 0.47 and remains in the range of FM in Figure 1a. The ratio increases abruptly to 0.66 for V_G = –5.0 V, driving the sample to the AFI phase region (Figure 1a) with an insulating feature at temperatures lower than 80 K (Figure 1b).

The suppression of conductivity and magnetism by gate voltages due to the Mn valence variation indicated the existence of phase separation. We now address the question of how the mixed phases behave in magnetic fields. Concomitant magnetization and magnetoresistance (MR) curves of LSMO under different gate voltages are obtained at 10 K (**Figure 3**). The maximum point in the MR curve of the pristine sample suggests that the coercivity of LSMO is 0.16 kOe (left axis of Figure 3a), which is corroborated by the magnetization loop (right axis of Figure 3a). MR and corresponding magnetization curves under a series of gate voltages are shown in Figure 3b–g. When V_G

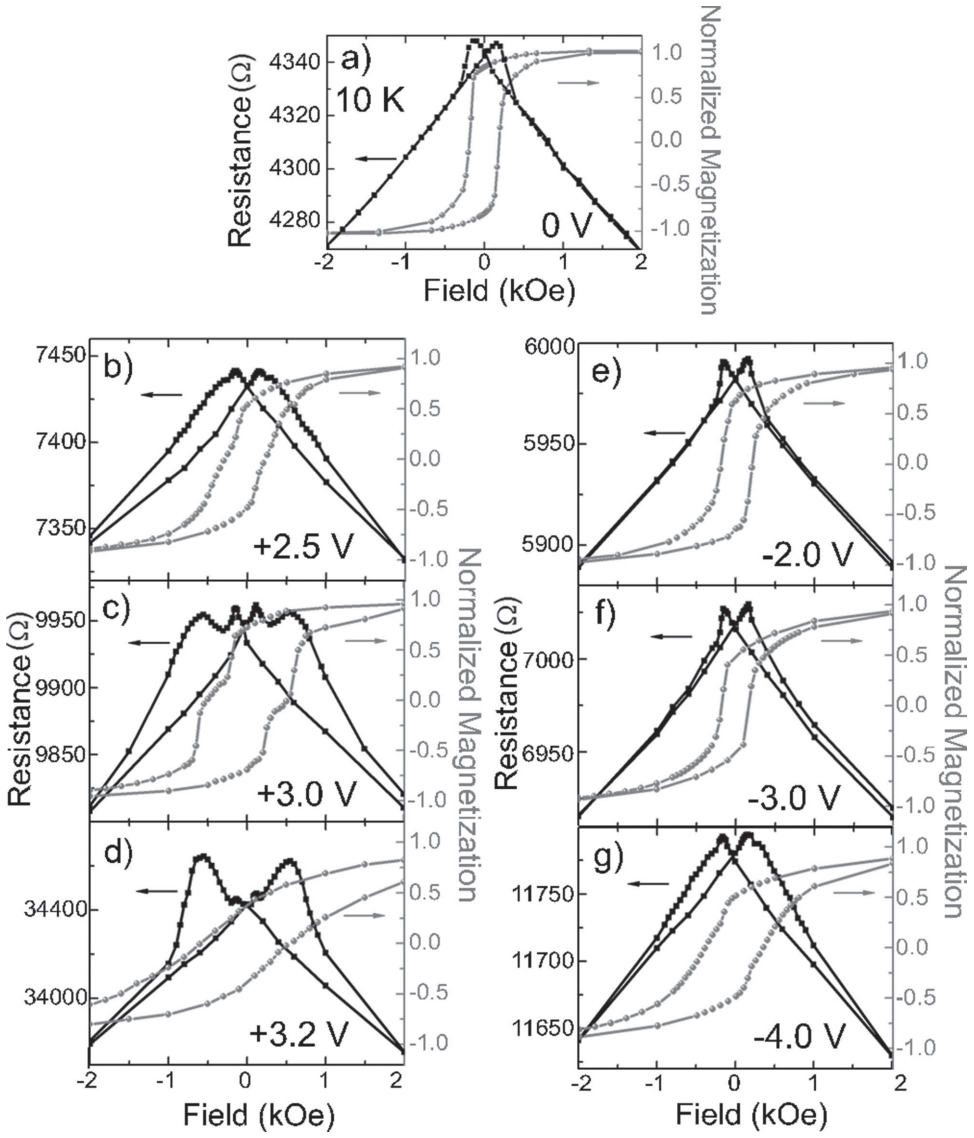

Figure 3. Channel MR acquired by sweeping the magnetic field along the channel (left axis) and the normalized magnetization curves measured with the magnetic field applied in-plane along the (100) direction of the substrate at 10 K (right axis) under different V_G: a) 0 V, b) +2.5 V, c) +3.0 V, d) +3.2 V, e) −2.0 V, f) −3.0 V, g) −4.0 V.

reaches +2.5 V, a subtle secondary switching at a higher field in the magnetization loop is observed, followed by the broadening of the MR curve in the high magnetic field direction. The most eminent feature observed here is that two broader peaks at ±0.55 kOe are superimposed besides the spikes at ±0.16 kOe, accompanied by an increase in resistance at V_G = +3.0 V. The corresponding hysteresis loop exhibits apparent dual coercivities (right axis in Figure 3c) at 0.16 kOe and 0.55 kOe. The carrier localization effect in the insulator increases the screening length of the electric field, and the HMI phase expands promptly as V_G further increases to +3.2 V, giving rise to the coercivity of 0.55 kOe in the LSMO, with a high resistance of ≈34 kΩ (Figure 3d). Indeed, +3.0 V is the critical V_G to excite the ferromagnetic PT in LSMO from soft FM into the hard magnetic insulating (HMI) phase, consistent with the ferromagnetic insulating (FI) phase in the region of low hole doping (Figure 1a). An even larger V_G (e.g., +3.5 V) leads to a highly insulating state beyond the measurement limits (Figure 1b).

Compared with the scenario of positive V_G, the amplitude of manipulation is dramatically reduced under negative V_G (–2.0 V and –3.0 V), as reflected in the MR and magnetization curves in Figure 3e,f, respectively. However, the situation changes abruptly once the hole concentration reaches the threshold of the antiferromagnetic insulating (AFI) phase region, e.g., in the case of V_G = –4.0 V illustrated in Figure 3g. An insulating phase emerges in the sample, exhibiting a resistance of 12 kΩ, with broadened peaks in the MR curve and a canted magnetization loop. In addition, as the double exchange effect is suppressed in the AFI manganite, no MR signal except for noise is observed for V_G = –5.0 V (not shown here). In contrast to the metal-insulator transition observed in correlated oxide previously,[14–16] the two separated phases with different conductive

behaviors here are ferromagnetic, exhibiting notable responses to the magnetic field.

To investigate the distribution of the HMI phase we now attempt to directly characterize the formation and annihilation of the HMI phase. First, note that no clear shift of the Mn 2*p* peaks is observed in the XPS depth profile (Figure S7 in the Supporting Information), proving that the HMI phase is randomly distributed in the films. Next, high-resolution transmission electron microscopy (HRTEM) characterization is used to directly image the distribution of the HMI phase. Based on the fact that the electric field effect is stable even after removing the V_G (Figure S3 in the Supporting Information), the films formerly treated by specific V_G are prepared into HRTEM specimens.

Representative HRTEM Fourier-filtered images with different V_G are presented in **Figure 4**a–d, while the original HRTEM images and the corresponding mechanism for the Fourier-filtered image are shown in Figure S8 in the Supporting Information. The Fourier-filtered image for the alignment of (100) planes of pristine LSMO and STO, as demonstrated in Figure 4a, indicates that there are no obvious crystal defects. The situation is different when V_G = +3.0 V (Figure 4b). The areas marked with the dashed ovals contain quite a few clearly recognizable dislocations (highlighted by ⊥), corresponding to the HMI phases with rich point defects, that is, oxygen vacancies induced by the electric field, which could assemble to form the line defects such as dislocations (see Figure S10 in the Supporting Information for more details).[22] Although the oxygen vacancies migration is not directly observed, the Mn valence variation in XPS and microstructure evolution in HRTEM under different gate voltages suggest the formation and annihilation of oxygen vacancies.[14] This is also supported by the demonstration of oxygen vacancies-based conduction filaments for resistive switching behaviors, based on the cutting-edge nano-characterization methods[23,24] and theoretical calculations.[25] The HMI phase is most likely concentrated around the area with a high density of dislocations, where the magnetization switching would be pinned by the defects.[26] Although it is likely that no oxygen vacancies could emerge for V_G = –5.0 V, the transition from Mn^{3+} (r = 0.65 Å) to Mn^{4+} (r = 0.53 Å) could also explain the existence of defects in the films. Note that this direct observation convincingly demonstrates that the HMI phase is randomly embedded in the matrix, rather than concentrating in specific regions such as the surface or the bottom of the films, which is compatible with the XPS depth profiling results. Interestingly, the crystal quality of the films after a sequence of V_G = +3.0 → –3.0 V is almost unchanged compared with its pristine counterpart, indicating that a negative voltage could drive the HMI → FM phase transition in turn. The crystal structure alternation undergoing such a gating process is reaffirmed by the X-ray diffraction characterization (Figure S9 in the Supporting Information).

The magneto-transport and magnetization measurements reveal the evolution of the HMI phase as a function of the gate voltage, while the XPS and HRTEM analyses indicate that the HMI phase is randomly embedded in the soft FM matrix, which is similar to the common lateral phase separation in manganites.[6] These characterizations collectively provide a novel explanation of the electronic PT in conductive manganites under the influence of the electric field effect. Figure 4e illustrates that the HMI phase undergoes a process of nucleation and growth: i) The screening length of the electric field in a metallic channel is less than 1 nm,[27] limiting the effect of electron doping only on the surface of the LSMO for the case of $V_G \leq$ +2.5 V; ii) The increase in positive gate voltages transforms the surface LSMO to the insulating state, which enlarges the screening length of the electric field and accelerates the PT in the sample by modulating the oxygen vacancies. In particular, electrons tend to gather around the intrinsic insulating spots, possibly formed during LSMO deposition,[6,15] giving rise to the local preferential growth of the HMI phase due to the conceptual carrier localization effect with high densities of Mn^{3+} and dislocation (V_G = +3.0 and +3.2 V).[15] iii) Once the channel is filled by the HMI phase, the strong electric field effect produces a highly

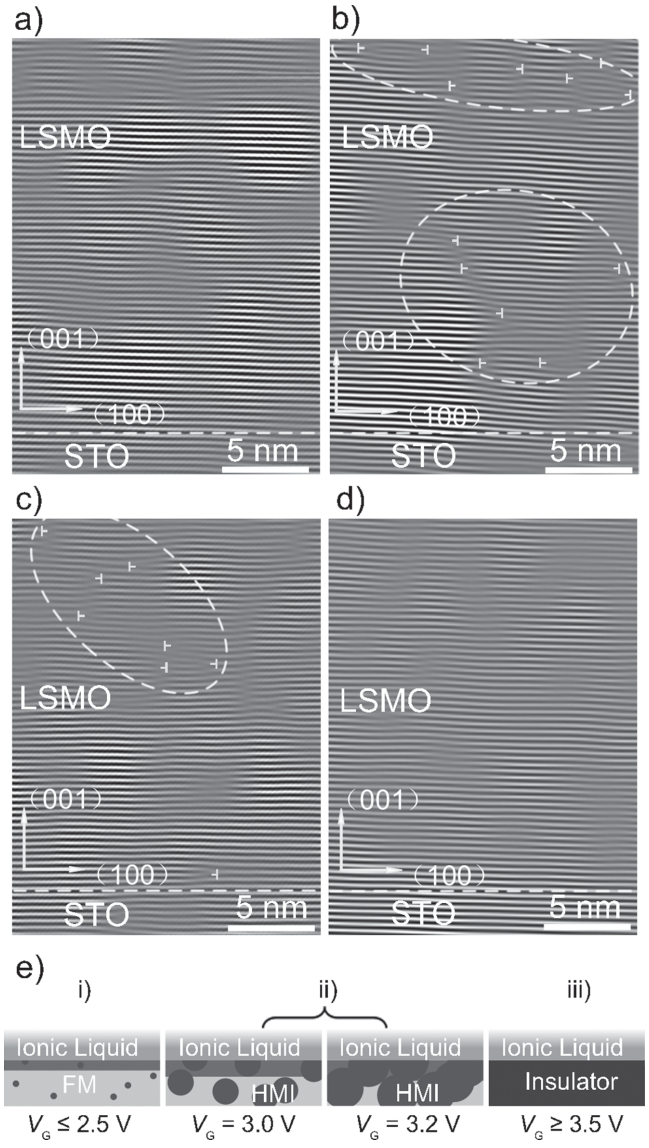

Figure 4. Fourier-filtered images of LSMO with different gate voltages and growth model for HMI phase: a) V_G = 0 V, b) V_G = +3.0 V, c) V_G = –5.0 V, and d) V_G = +3.0 → –3.0 V. The ⊥ and dashed ovals mark the dislocation and estimated areas with high dislocation density, respectively. e) Schematic of the growth of the HMI phase with different gate voltages.

insulating character ($V_G \geq +3.5$ V), which is almost irreversible, even with a negative voltage.

It is generally considered that a channel under electric field modulation could be treated as two parallel layers: the layer near the gate-channel interface is effectively affected by electrostatic doping, whereas the layer underneath remains unaffected.[13,16] Here, we improve this model by providing direct experimental evidence of the random nucleation and growth of the HMI phases across the film, thus enabling the proposal of a conceptually novel model of the phase transition tuned by the electric field. This novel model, moreover, can be readily generalized in other correlated electron systems. In addition, we determine the fraction of the HMI phase as a function of the gate voltages and temperatures in a quantitative manner (see Figure S11 in the Supporting Information), revealing that the HMI phase fraction reaches its maximum at approximately 260 K, which is consistent with the Curie temperature measurements in Figure 1b.

Based on the microstructure characterization and property measurement, the HMI phase can be annihilated by a negative V_G; therefore, it is promising to realize the FM/HMI phase transition reversibly by electrical manipulation. **Figure 5**a illustrates the V_G dependence of the channel resistance measured at $T = 260$ K, which is lower than the T_C of ferromagnetic LSMO but higher than the condensation temperature of ionic liquid. In these measurements, V_G is changed in the sequence of +3.0 V → –5.0 V → +3.0 V (indicated by the arrows) with a step of 0.5 V. The resistance is recorded after the gate voltage is applied for 30 min. Under no external magnetic field (H), as the V_G decreases from +3.0 V to 0 V, the channel resistance decreases slowly from 23.9 kΩ to 22.7 kΩ, where the HMI phase dominates. As the voltage is swept down, the resistance decreases sharply to 16.3 kΩ when $V_G = -3.5$ V, suggesting that the accumulated electrons are "neutralized" by the negative voltages in a HMI → FM transition ("I" in Figure 5a). We note that the LSMO at this stage is close to the pristine state. However, as V_G further decreases to –5.0 V, excessive holes are injected into the manganite layer, driving the resistance up to 20.8 kΩ (II). For the voltage sweep in reverse (–5.0 V → +3.0 V), the resistance is reduced from 20.8 kΩ (–5.0 V) to 16.9 kΩ (+1.0 V) first (III) and then increases to 25.6 kΩ (+3.0 V) (IV). The closed electroresistance (ER) loop proves that the electronic PT and the resulting resistance transition are reversible with a hysteresis feature. By adding the CMR nature of manganites to the reversible ER behavior, it is possible to achieve the four nonvolatile states in such systems. As expected, once a magnetic field $H = 5$ kOe is applied, the channel resistance loop exhibits nearly the same shape as that at zero field but with a reduced resistance. This result illustrates that the LSMO channel gated by ionic liquid is a four-state non-volatile memory cell, where four resistance values can be achieved by a given V_G sweep process and an applied magnetic field.

To examine the stability and repeatability of the PT, subsequent gate voltage pulses of ±3 V are applied to manipulate the ER of the LSMO, as displayed in the upper panel of Figure 5b. For each voltage pulse, the holding time is approximately 15 min, and only 2~3 min is required to obtain a relative stable channel resistance (Figure S3 in the Supporting Information). The lower panel of Figure 5b presents the concomitant

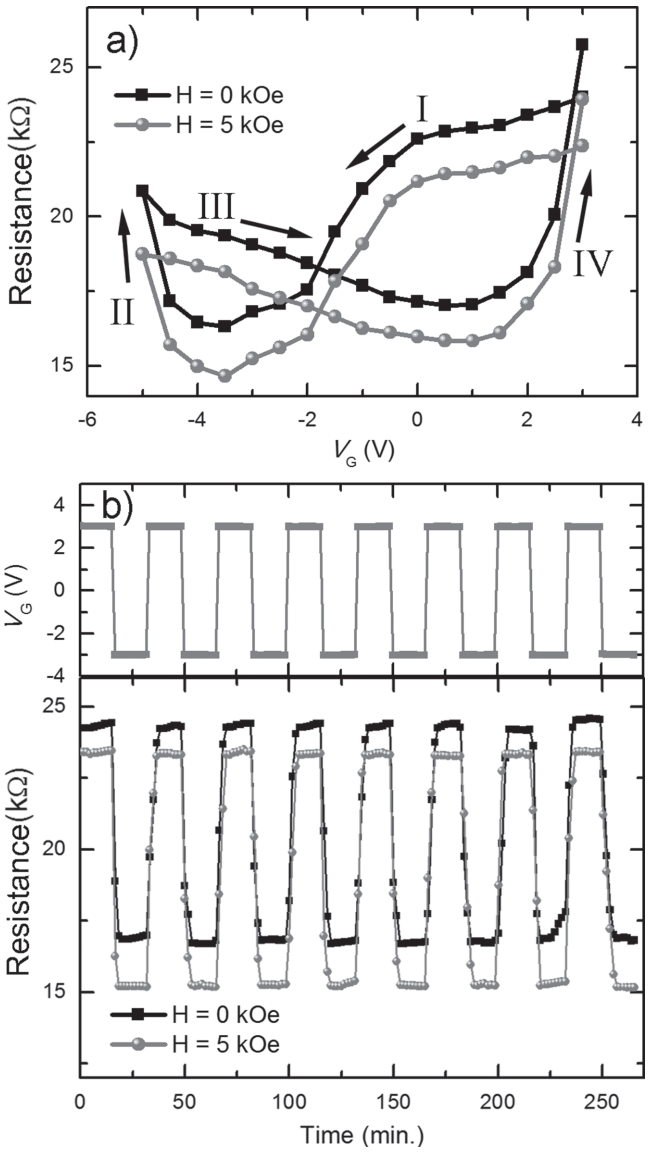

Figure 5. a) Channel resistance versus V_G with $H = 0$ kOe and 5 kOe. b) Channel resistance as a function of time under a ±3.0 V voltage pulse with $H = 0$ kOe and 5 kOe. The top panel is the schematic of the applied gate voltage versus time.

resistance response at zero-field and 5 kOe measured at 260 K. Given that the FM/HMI transition is motivated by the gate voltage, a positive gate voltage +3.0 V introduces the HMI phase with a high resistance in the manganite, while a negative $V_G = -3.0$ V neutralizes the electrons in the channel and reduces their resistance, resulting in an ER% = 45.3% and 53.5% for $H = 0$ kOe and 5 kOe, respectively, essentially undergoing process "I" in Figure 5a. Here, ER% is defined as $(R_{high}-R_{low})/R_{low}$, where R_{high} and R_{low} are resistances at $V_G = +3.0$ and –3.0 V, respectively. Simultaneously, the magnitude of magnetoresistance [MR% = $(R_{5\ kOe}-R_0)/R_0$] varies from –3.9% to –9.1% as V_G is switched from +3.0 to –3.0 V. The ferromagnetic phase transition induced by application of the gate voltage, which differs drastically from the generally observed metal-insulator transition,[13,14] guarantees that the system exhibits a remarkable

response to the magnetic field as well, thus providing a rich platform for multilevel storage. Such a reversible PT with stable ER and MR could be manipulated near 300 K, which promises future room temperature operations after further optimization. Note that the modification time (2–3 min) here is much longer than the requirement of information storage but is acceptable for sensors. The modification time promises to be dramatically reduced once a new type of ionic liquid with higher working speed is synthesized.

3. Conclusions

In conclusion, electronic phase separation in LSMO was successfully controlled by an electric field applied on the ionic liquid, replicating the tendency in the classic phase diagram based on the Sr doping concentration in $La_{1-x}Sr_xMnO_3$. A suitable gate voltage was proven to generate a hard magnetic and insulating phase in the magnetically soft matrix, which is theoretically different from the simple metal-insulator transition induced by the electric field. We combined the direct observation of the formation and annihilation of the HMI phase, followed by the variation in the $Mn^{4+}/(Mn^{3+}+Mn^{4+})$ ratio and dislocation density, with magneto-transport and magnetization measurements, demonstrating that the HMI phase is randomly embedded all over the film instead of initiating at the surface and spreading to the bottom. The reversible ferromagnetic phase transition not only enables a new realm for recognition of the origin and process of the phase transition in correlated oxides but also sheds promising light on the metal-insulator transition in colossal magnetoresistance materials. The observation of the four-state memories close to room temperature controlled by a combination of electrode gating and magnetic field represents a significant opportunity for the application of electrical control of magnetism for multilevel storage approaches.

4. Experimental Section

Sample Preparation: All of the samples were grown using pulsed laser deposition (PLD) from a stoichiometric $La_{0.6}Sr_{0.4}MnO_3$ target by applying a KrF excimer laser. During the growth, the substrate was held at 800 °C and in an oxygen background pressure of 100 m Torr. The growth was monitored in situ using RHEED (reflection high-energy electron diffraction) analysis, which enables precise control of the thickness at the unit cell scale and accurate characterization of the growth dynamics. The films are grown in layer-by-layer mode according to the RHEED oscillations at a growth rate of 0.77 nm/min (Figure S1a in the Supporting Information). The samples were slowly cooled to room temperature in 100 Torr of oxygen at a rate of ≈5 °C/min to improve the oxidation level after growth. The film was patterned into a Hall-bar structure with a gate located in the vicinity of the channel by photo-lithography and wet etching, as shown in Figure S2 (Supporting Information). The effective channel is 600 μm long and 100 μm wide. All Ti (20 nm)/Au (80 nm) electrodes were deposited using electron-beam evaporation. Hard-baked photoresist was used for electrical isolation between the gate and the channel. A drop ionic liquid *N*,*N*-diethyl-*N*-(2-methoxyethyl)-*N*-methylammonium bis-(trifluoromethylsulfonyl)-imide (DEME-TFSI) was used as the electrolyte. Samples with large areas of 2.5 mm × 2.5 mm are required, and almost the entire film is gated by ionic liquid before the corresponding XPS, magnetization, HRTEM, and XRD measurements.

Sample Characterization: Conductivity and magnetoresistance were determined in the physical property measurement system (PPMS) with a constant in-plane current of 10 μA. The gate voltage was applied using an Agilent 2901A instrument. All of the transport experiments were performed after maintaining V_G for 30 min without special instruction. A Quantum Design superconducting quantum interference device (SQUID) measurement system (QD MPMS-7) was used to measure the magnetic properties along the (100) direction of the substrate in the temperature range of 10 K to 350 K.

Supporting Information

Supporting Information is available from the Wiley Online Library or from the author.

Acknowledgements

The authors are grateful to Prof. R. Yu and S. B. Cheng of Beijing National Center for Electron Microscopy and Center for Testing & Analyzing of Materials of Tsinghua University for technical support. This work was supported by the National Natural Science Foundation of China (Grant Nos. 51322101, 51202125 and 51231004), National Hi-tech (R&D) project of China (Grant no. 2014AA032904, 2014AA032901 and 2013AA030801) and National Basic Research Program of China (Grant No. 2010CB832905).

Received: June 18, 2014
Revised: August 2, 2014
Published online: September 8, 2014

[1] A. Moreo, S. Yunoki, E. Dagotto, *Science* **1999**, *283*, 2034.
[2] C. H. Ahn, A. Bhattacharya, M. D. Ventra, J. N. Eckstein, C. D. Frisbie, M. E. Gershenson, A. M. Goldman, I. H. Inoue, J. Mannhart, A. J. Millis, A. F. Morpurgo, D. Natelson, J. M. Triscone, *Rev. Mod. Phys.* **2006**, *78*, 1185.
[3] J. M. D. Coey, M. Viret, S. von Molnár, *Adv. Phys.* **1999**, *48*, 167.
[4] P. H. Xiang, S. Asanuma, H. Yamada, I. H. Inoue, H. Sat, H. Akoh, A. Sawa, K. Ueno, H. T. Yuan, H. Shimotani, M. Kawasaki, Y. Iwasa, *Adv. Mater.* **2011**, *23*, 5822.
[5] B. Cui, C. Song, G. Y. Wang, H. J. Mao, F. Zeng, F. Pan, *Sci. Rep.* **2013**, *3*, 2542.
[6] T. Becker, C. Streng, Y. Luo, V. Moshnyaga, B. Damaschke, N. Shannon, K. Samwer, *Phys. Rev. Lett.* **2002**, *89*, 237203.
[7] J. J. Peng, C. Song, B. Cui, F. Li, H. J. Mao, Y. Y. Wang, G. Y. Wang, F. Pan, *Phys. Rev. B* **2014**, *89*, 165129.
[8] H. Ohno, D. Chiba, F. Matsukura, T. Omiya, E. Abe, T. Dietl, Y. Ohno, K. Ohtani, *Nature* **2000**, *408*, 944.
[9] S. Ikeda, K. Miura, H. Yamamoto, K. Mizunuma, H. D. Gan, M. Endo, S. Kanai, J. Hayakawa, F. Matsukura, H. Ohno, *Nat. Mater.* **2010**, *9*, 721.
[10] D. Chiba, S. Fukami, K. Shimamura, N. Ishiwata, K. Kobayashi, T. Ono, *Nat. Mater.* **2011**, *10*, 853.
[11] Y. Yamada, K. Ueno, T. Fukumura, H. T. Yuan, H. Shimotani, Y. Iwasa, L. Gu, S. Tsukimoto, Y. Ikuhara, M. Kawasaki, *Science* **2011**, *332*, 1065.
[12] H. S. Lee, S. G. Choi, H. H. Park, M. J. Rozenberg, *Sci. Rep.* **2013**, *3*, 1704.
[13] M. Nakano, K. Shibuya, D. Okuyama, T. Hatano, S. Ono, M. Kawasaki, Y. Iwasa, Y. Tokura, *Nature* **2012**, *487*, 459.
[14] J. Jeong, N. Aetukuri, T. Graf, T. D. Schladt, M. G. Samant, S. S. P. Parkin, *Science* **2013**, *339*, 1402.
[15] J. Lourembam, J. C. Wu, J. F. Ding, W. N. Lin, T. Wu, *Phys. Rev. B* **2014**, *89*, 014425.

[16] A. S. Dhoot, C. Israel, X. Moya, N. D. Mathur, R. H. Friend, *Phys. Rev. Lett.* **2009**, *102*, 136402.
[17] I. H. Inoue, M. J. Rozenberg, *Adv. Funct. Mater.* **2008**, *18*, 2289.
[18] H. Yamada, Y. Ogawa, Y. Ishii, H. Sato, M. Kawasaki, H. Akoh, Y. Tokura, *Science* **2004**, *305*, 646.
[19] H. W. Nesbitt, D. Banerjee, *Am. Mineral.* **1998**, *83*, 305.
[20] T. Hishida, K. Ohbayashi, T. Saitoh, *J. Appl. Phys.* **2013**, *113*, 043710.
[21] D. Lee, J. H. Lee, P. Murugavel, S. Y. Jang, T. W. Noh, Y. Jo, M. H. Jung, Y. D. Ko, J. S. Chung, *Appl. Phys. Lett.* **2007**, *90*, 182504.
[22] C. Song, S. N. Pan, X. J. Liu, X. W. Li, F. Zeng, W. S. Yan, B. He, F. Pan, *J. Phys.: Condens. Matter* **2007**, *19*, 176229.
[23] J.-Y. Chen, C.-L. Hsin, C.-W. Huang, C.-H. Chiu, Y.-T. Huang, S.-J. Lin, W.-W. Wu, L.-J. Chen, *Nano Lett.* **2013**, *13*, 3671.
[24] F. Pan, S. Gao, C. Chen, C. Song, F. Zeng, *Mater. Sci. Eng. R* **2014**, *83*, 1.
[25] M. J. Rozenberg, M. J. Sánchez, R. Weht, C. Acha, F. Gomez-Marlasca, P. Levy, *Phys. Rev. B* **2010**, *81*, 115105.
[26] K. He, D. J. Smith, M. R. McCartney, *Appl. Phys. Lett.* **2005**, *86*, 142501.
[27] X. Hong, A. Posadas, C. H. Ahn, *Appl. Phys. Lett.* **2009**, *95*, 182507.